

# Acoustic Metal

Mengyao Xie, Min Yang,\* Songwen Xiao, Yunfei Xu, and Shuyu Chen<sup>†</sup>  
*Acoustic Metamaterials Group Ltd. Genesis, 33-35 Wong Chuk Hang Rd. Hong Kong, China*

Metal reflects electromagnetic waves because of the large conductivity that is responsible for dissipation. During which the waves undergo a  $180^\circ$  phase change that is independent of the frequency. There is no counterpart material for acoustic waves. Here we show that by using an array of acoustic resonators with a designed high-density dissipative component, an “acoustic metal” can be realised that strongly couples with sound over a wide frequency range not otherwise attainable by conventional means. In particular, we show the acoustic Faraday cage effect that when used as a ring covering an air duct, 99% of the noise can be blocked without impeding the airflow. We further delineate the underlying volume requirement for an acoustic metal based on the constraint of the causality principle. Our findings complement the missing properties of acoustic materials and pave the way to the strong wave-material couplings that are critical for the applications as high-performance audio devices.

## I. INTRODUCTION

Large dissipation coefficient does not always lead to effective energy absorption. The best example is metal, which has a large conductivity but reflects the electromagnetic (EM) waves strongly<sup>1</sup>. Such reflections are noted to be nearly  $180^\circ$  out of phase with the incident wave and independent of the frequency. While in recent years resonance-based acoustic metamaterials<sup>2-5</sup> have achieved exceptional material properties, including zero and negative parameters<sup>6-12</sup>, chiral micropolar behaviour<sup>13-15</sup>, nonreciprocity by a magnetic-like circular flow<sup>16-18</sup>, and exotic absorptions<sup>19</sup>, there is still no “acoustic metal” that reflects sound in the same way as metal reflects EM waves. This is due to the very high contrast between the solid and air impedance that prevents the effective coupling and damping in broadband. Recently, by a designed integration of multiple acoustic resonators, broadband near-perfect absorption was achieved<sup>20-28</sup>. In this work, we push the dissipative component of the resonator array an order of magnitude higher so that the structure becomes an acoustic metal that reflects sound waves instead of absorbing them. In analogy to the metallic mesh that shields the microwaves from leaking out of the microwave oven or the Faraday cage for shielding the EM waves, a circular ring of such acoustic metal, lining the inner wall of a short air duct ( $\sim 4$  cm), is shown to block almost all the low-frequency noise within an octave. Such blocking effect evidences the strong couplings with sound.

In what follows, Section II presents a “phase diagram” to position the acoustic metal in relation to other acoustic materials as characterised by their impedance. In Section III we describe the design strategy for the acoustic metal, followed by the presentation of experimental results in Section IV. The underlying volume requirement for an acoustic metal, in relation to its effective frequency range, is described in Section V. We conclude with a short recapitulation in Section VI.

## II. ACOUSTIC METAL AND THE SOFT BOUNDARY

By denoting the specific acoustic impedance of the air by  $Z_0$ , the displacement velocity on sample’s surface equals to

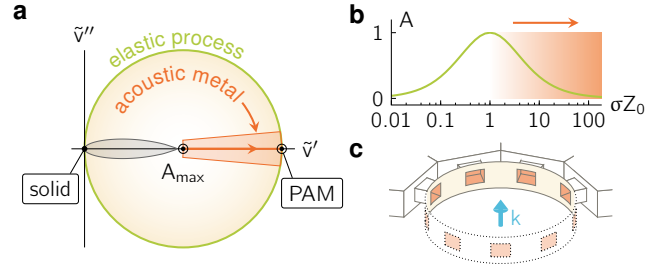


FIG. 1. Acoustic metal. **a**, Normalised by the displacement velocity of the incident sound  $v_i$ ,  $\tilde{v} = v/v_i$  of all the different sample responses forms a circle on the complex plane  $\tilde{v} = \tilde{v}' + i\tilde{v}''$ . Most of the solid materials are around the origin with the acoustic foam extending to the centre (the grey region). In contrast, acoustic metals are in the red shaded section in which the reflection is  $180^\circ$  out of phase with the incident wave. Perfect acoustic metal (PAM) is at the limit of  $\tilde{v} = 2$ . The colour gradient maps the relevant absorption coefficient. At the green-coloured circumference the absorption is zero. Absorption is maximised at the centre of the circle. **b**, The absorption as a function of the acoustic conductivity  $\sigma$  (normalised to the inverse of the specific air impedance  $Z_0$ ), plotted along the real axis in **a**.  $A_{\max}$  is at  $\sigma Z_0 = 1$ . Acoustic conductivity  $\sigma \rightarrow \infty$  for PAM. **c**, Like the metallic mesh shielding the EM waves, the acoustic metals (the structured cavities) covering the inner wall of an air duct (the circular cylinder) can block the sound, indicated here by the blue arrow, without impeding the airflow.

the superposition of the particle velocities of the incident and reflected waves,  $v = p_i/Z_0 - p_r/Z_0$ . Here,  $p_i$  and  $p_r$  are the respective incident and reflected sound wave pressure modulations and the negative sign is due to their opposite propagating directions. Conservation of energy dictates that  $|p_r| = |p_i - vZ_0| \leq |p_i|$  which corresponds to the dimensionless  $\tilde{v} = vZ_0/p_i$  inside a circle of radius 1 on the complex plane  $\tilde{v} = \tilde{v}' + i\tilde{v}''$ ,

$$|\tilde{v} - 1| \leq 1,$$

as shown in Figure 1a. This circle can serve as a “phase diagram” to represent the distinct motions of the various sample materials in response to the incident sound wave. At the origin is the motionless hard boundary. Along the circular edge, coloured by green, the total pressure  $p = p_i + p_r =$

$2p_i - vZ_0 = (2 - \tilde{v})p_i$  always differs from  $v$  by a phase of  $\pi/2$ , hence lossless. At the far right of the circle,  $p$  approaches zero for the condition of soft boundary, at which point  $\tilde{v} = 2$  reaches its maximum magnitude implying the maximum coupling with sound. From the circumference of the circle the absorption coefficient

$$A = 1 - |p_r/p_i|^2 = 1 - |\tilde{v} - 1|^2 \quad (1)$$

monotonously increases (indicated by the colour gradient) as a function of decreasing radial distance to the centre and reaches the maximum absorption  $A_{\max}$  at  $\tilde{v} = 1$  (i.e., the impedance-matching condition). Most of the solid materials are around the origin while the porous acoustic materials such as foam and wool extend to the centre of the circle along the real axis (the grey region)<sup>19</sup>.

Since a metal is characterised by its high conductivity for dissipation,  $\sigma$ , hence in analogy we introduce the acoustic conductivity and permittivity as  $v = (\sigma - i\omega\varepsilon)p$ .<sup>29</sup> Under the incident sound with pressure modulation  $p_i$ ,  $p = 2p_i - vZ_0$  so that the dimensionless

$$\tilde{v} = \frac{2Z_0}{1/(\sigma - i\omega\varepsilon) + Z_0}, \quad (2)$$

which is along the real axis in Figure 1a, provided  $\omega\varepsilon \ll \sigma$  is negligible as that in a metal. Furthermore, to have the reflection,  $p_r$ , 180 degrees out of phase with  $p_i$ , where  $p_r = (1 - \tilde{v})p_i = p_i(1 - \sigma Z_0)/(1 + \sigma Z_0)$ ,  $\sigma$  also has to meet another requirement that  $\sigma > 1/Z_0$ . Combining the above two conditions, we can delineate the section coloured in red in Figure 1a as the region for acoustic metals. This region is noted to be far beyond the scope of the conventional acoustic materials coloured by grey. In Figure 1b we show that the absorption has a peak when  $\sigma = 1/Z_0$ ; with the growth of  $\sigma$  the perfect acoustic metal (PAM) limit is approaching when  $\sigma \rightarrow \infty$  at the soft boundary limit of (the dimensionless  $\tilde{v} = 2$ ). In Figure 1c we illustrate the geometry of the acoustic metal resonator array intended to realise the acoustic counterpart to the Faraday cage effect for the EM waves.

### III. DESIGN STRATEGY

Our strategy is to design an array comprising a large number of resonators within a sub-wavelength scale so that the resonators respond in unison. While the response of each of the resonators can be delineated mathematically by the Lorentzian form, the array as a whole would respond as an acoustic metal as shown below.

Consider an array of resonators whose resonance frequencies are uniformly distributed. The oscillatory nature of the individual  $\varepsilon_n$  may tend to cancel each other while, in contrast, the individual  $\sigma_n$  are always positive and can accumulate. As a result, the overall permittivity becomes small while the conductivity can increase to a large value that is approximately constant in frequency as desired.

Mathematically, the velocity of the  $n$ th resonator is given

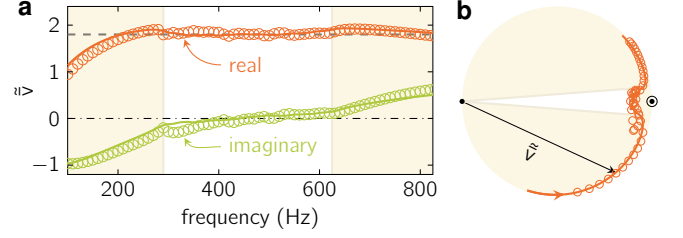


FIG. 2. The surface displacement velocity of acoustic metal. **a**, The averaged dimensionless velocity of the acoustic metal,  $\tilde{v} = \tilde{v}' + i\tilde{v}''$ , plotted as a function of frequency. Within the designed frequency band (region without shading),  $\tilde{v}'' \rightarrow 0$  (green) while  $\tilde{v}'$  (red) is close to the target values (dashed) when  $\bar{\sigma}Z_0 = 9$  and  $\bar{\varepsilon} = 0$ . **b**, On the complex plane, the magnitude of  $\tilde{v}$  in the designed frequency band (region with no shading) are noted to be closely distributed around the PAM limit. The red arrow points to the direction of increasing frequency. In both **a** and **b**, the solid curves are theoretical predictions from Equation (4) and the open circles are retrieved from experimental data of a real sample shown in Figure 3.

by<sup>30</sup>

$$v_n = \frac{-i\omega f_n}{\omega_n^2 - \omega^2 - i\omega\beta_n} p = (\sigma_n - i\omega\varepsilon_n)p \quad (3)$$

with  $\omega_n(f_n)$  being its resonant frequency(oscillator strength), and  $\beta_n$  the damping coefficient. Denoting its surface area by  $a_n$ , only the averaged  $\bar{v} = \sum_n a_n v_n / \sum_n a_n$  over all the resonators can couple to the propagating waves, owing to the sub-wavelength nature of the array. Hence  $p = 2p_i - \bar{v}Z_0$  in Equation (3). Together with the definition of  $\bar{v}$ , we obtain an expression similar to Equation (2):

$$\bar{v} = \frac{\bar{v}}{p_i/Z_0} = \frac{2Z_0}{1/(\bar{\sigma} - i\omega\bar{\varepsilon}) + Z_0}. \quad (4)$$

In Equation (4) the averaged  $\bar{\sigma}$  and  $\bar{\varepsilon}$  of the composite are defined by

$$\bar{\sigma} = \frac{\sum_n a_n \sigma_n}{\sum_n a_n} = \frac{\omega^2}{\sum_n a_n} \sum_n \frac{a_n f_n \beta_n}{(\omega_n^2 - \omega^2)^2 + \omega^2 \beta_n^2}, \quad (5a)$$

$$\bar{\varepsilon} = \frac{\sum_n a_n \varepsilon_n}{\sum_n a_n} = \frac{1}{\sum_n a_n} \sum_n \frac{a_n f_n (\omega_n^2 - \omega^2)}{(\omega_n^2 - \omega^2)^2 + \omega^2 \beta_n^2}. \quad (5b)$$

Equation (5a) shows that indeed, the averaged  $\bar{\sigma}$  can accumulate and become large in magnitude whereas the summed terms in Equation (5b) are always opposite in sign between adjacent  $\omega_n$ , hence cancelling each other.

For a uniformly distributed  $\omega_n$  each separated from the neighbours by a small  $\delta\omega = \omega_n - \omega_{n-1}$ , we wish to focus on the two parameter  $f_n$  and  $\beta_n$  that are crucial to the acoustic metal design. In the limit of  $\delta\omega \rightarrow 0$ , the summation in Equation (5a) becomes an integral that gives  $f_n \simeq \bar{\sigma} \times 2\delta\omega \sum_n a_n / (\pi a_n)$ .<sup>31</sup> Since large  $\bar{\sigma}$  of acoustic metal requires large displacement velocity, we show in Appendix A that, in contrast to the displacement velocity of a single Lorentz resonator which is suppressed by the damping,

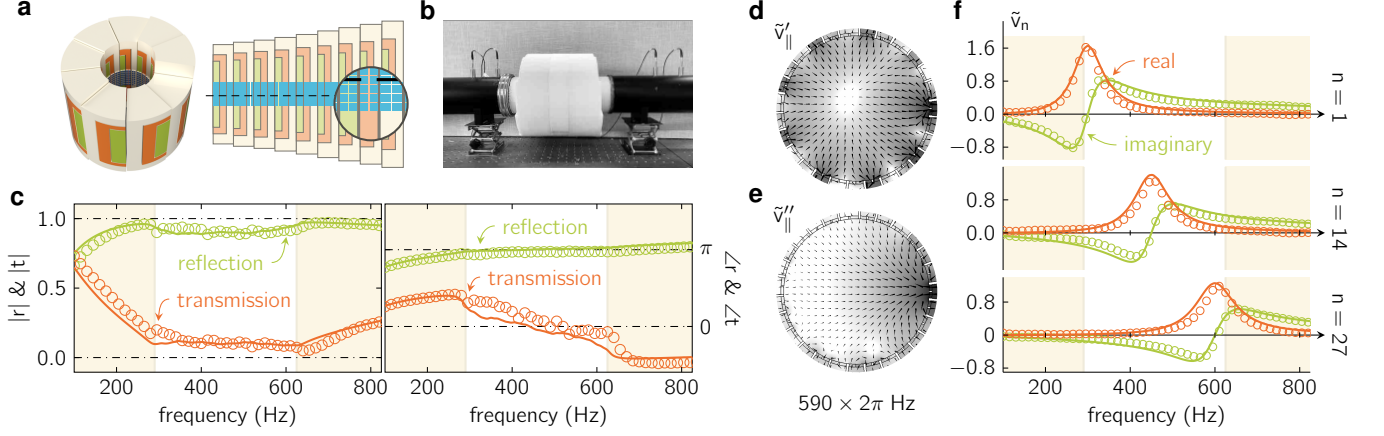


FIG. 3. The acoustic metal structure comprises an array of Helmholtz resonators (HRs). **a**, 27 HRs formed a compact structure lining the inner wall of an air duct. The projected pattern of their cavities and necks (the magnified blue rectangles) is shown by the 2D schematics. **b**, A photo image of the sample and relevant experiment setups. **c** The amplitude and phase of the reflectance  $r$  and transmittance  $t$ . Within the designed frequency band (the region without shading), the transmitted energy is only about  $|t|^2 \sim 1\%$  with the reflection phase around  $\angle r \sim \pi$ . **d** and **e**, The simulated, normalised particles' in-plane velocity fields,  $\tilde{v}_{\parallel} = \tilde{v}'_{\parallel} + i\tilde{v}''_{\parallel}$ , plotted on the cross-section marked in **a** by the dashed line.  $\tilde{v}'_{\parallel}$  and  $\tilde{v}''_{\parallel}$  have distinct topology features in which  $\nabla \cdot \tilde{v}_{\parallel} \neq 0$  indicates the out-plane couplings caused by the HRs. **f**, The  $\tilde{v}_n$  of the individual HRs when the other 26 were closed. Three examples have been chosen as  $n = 1, 14, 27$ . All the solid curves are the theoretically calculated targets and the open circles are the data from experiments.

the collective summation of the array resonators' dissipative component can lead to the overall  $\tilde{v}$  increases with the damping as long as  $\beta_n$  does not exceed  $2\delta\omega$ .

In the following, we design the acoustic metal by targeting  $\bar{\sigma} = 9/Z_0$  over a broad frequency band from 290 to 625 Hz. If there are 27 resonators,  $\delta\omega = 12.9 \times 2\pi$  Hz and  $f_n Z_0 \times a_n / \sum_n a_n = 464.4$  Hz. Therefore, by choosing  $\beta_n = 2\delta\omega$ , as shown in Figure 2a by the solid curves, Equation (4) predicted that  $\tilde{v}' \gg \tilde{v}''$  within the designed frequency band (the blank region) with the value of  $\tilde{v}'$  close to the target values (dashed line) when  $\bar{\sigma} = 9/Z_0$  and  $\bar{\varepsilon} = 0$ . In the phase-diagram shown in Figure 2b, all the vectors of the dimensionless complex velocities between 290 and 625 Hz are noted to fall into a sector that has no shading. It is clear that they were mostly in the acoustic metal phase as delineated in Figure 1a and tightly distributed around the PAM limit.

#### IV. EXPERIMENTAL REALISATION

We wish to demonstrate the effect of the acoustic metals by realising an acoustic counterpart to the Faraday cage effect that blocks EM waves through a layer of metallic mesh whose pores are smaller than the wavelengths. For simplicity, we consider only one pore of a mesh in practice, designed as a ring covering the inner wall of an air duct as shown in Figure 1c. The actual duct used in the demonstration has a cross-sectional area  $a = 78.5$  cm<sup>2</sup>. The specific impedance for the air in the duct is given by  $Z_0 = \rho c \sum_n a_n / (2a)$  (detailed in Appendix A), where  $\rho = 1.2$  kg/m<sup>3</sup> is the air density and  $c = 343$  m/s is the speed of airborne sound.

As shown in Figure 3a, the acoustic metal sample comprises 27 Helmholtz resonators (HRs) whose cavities share

the same depth of  $L = 74$  mm and each individual rectangular neck is connected to the central duct with the same length of  $l = 2$  mm. As an approximation, the resonance frequency of the  $n$ th HR is given by  $\omega_n = c\sqrt{a_n}/(A_n L l)$  with  $A_n = V_n/L$  being the effective cross-sectional area of the cavity and  $V_n$  being the cavity volume. The frequency  $\omega_n$  can be directly tuned by the areal ratio  $a_n/A_n$  so as to be uniformly distributed in the designed frequency band of (290,625) Hz while the desired values of  $f_n$  are obtainable from adjusting the specific  $A_n/a_n$  and  $A_n$  for our design are listed in Table I of Appendix A. By keeping these areas unchanged, we deformed their shapes so that the resonators can be assembled compactly. In order to attain a sufficiently large  $\beta_n$ , thin partitions were inserted into the necks so as to divide each into 16 parts (the tiny blue rectangles in Figure 3a), with the purpose of achieving larger air-solid interfaces, aimed to increase the acoustic dissipation.

We have fabricated the designed structure by the stereolithography 3D printing technology. To carry out the measurement, the sample was connected to two circular impedance tubes of the same inner diameter on the two sides as shown in Figure 3b. During the experiments, a loudspeaker continuously generates sinusoidal signals from one end. Two microphones on the front tube recorded the reflected sound,  $p_r$ , from the structure while another two microphones on the rear measuring the transmitted  $p_t$ . Acoustic foam was put at the rear end to insure there was no reflection. The results are shown in Figure 3c by open circles. Within the designed frequency band (the area without shading),  $|t| = |p_t/p_i| \sim 0.1$  (red) and  $|r| = |p_r/p_i| \sim 0.89$  (green) indicating that about 99% of the forward propagating energy has been blocked by the acoustic metal. The phase of reflection  $\angle r \simeq \pi$  in the designed frequency band that consistent with the signature of a

metal. Based on these experimental data, we can retrieve the values of  $\tilde{v}$  as shown by the open circles in Figure 2. Excellent agreement with the theoretical design target (solid curves) is seen. The relationship between  $\tilde{v}$ ,  $r$  and  $t$  is detailed in Appendix A.

Figures 3d and e show the numerically simulated in-plane air velocity field  $\tilde{v}_{\parallel} = v_{\parallel}/v_i$  on the duct cross-section, which intersects all the HRs' openings as denoted by the dashed line in Figure 3a. The two figures demonstrate in detail how the HRs attain their metallic behaviour by blocking the sound waves in the duct. For sound frequencies in the designed frequency band, e.g., at  $\omega = 590 \times 2\pi$  Hz, all the in-phase components, i.e. real parts, of the displacement velocity ( $\tilde{v}'$ ) vectors in Figure 3d are pointed towards the HRs, with a “source” of outward arrows at the centre. Such a source draws the air in the ducts from both sides of the plane so that, on the transmission side, the air displacement velocity is opposite to that of the incident wave's  $v_i$ , thereby cancelling it. Meanwhile, the out-of-phase component of the displacement velocity ( $\tilde{v}''$ ) vectors in Figure 3e presents a distinct feature that  $\nabla \cdot \tilde{v}'' \simeq 0$  everywhere—which means that the air expelled from the resonating HR is completely compensated by the intakes of the others with different resonance frequencies. Such in-phase and out-of-phase behaviours of the displacement velocity correspond exactly to the two equations in Equation (5).

Be noted that our simulations did not consider the airflow in the air duct since the airflow speed is usually only a few percent of the sound speed (wind tunnel being the exception), therefore only has a negligible effect.

The above conclusions can be further confirmed experimentally by individually measuring the 27 HRs by blocking the 26 resonators and retrieving the relevant normalised velocity  $\tilde{v}_n = v_n/v_i$  for the one not blocked. As illustrated by the three examples in Figure 3f, all the  $\tilde{v}'_n > 0$  (denoted by the red curves) confirms that the velocity is directed towards the relevant HRs in Figure 3d. In contrast, at any given frequency in the design band, all the HRs at those frequencies below the given frequency contribute positively to  $\tilde{v}''_n$  (green curves), and those at frequencies above the given frequency contributes negatively to  $\tilde{v}''_n$ . Such behaviour corresponds exactly to that indicated by Figure 3e.

## V. VOLUME REQUIREMENT

The conductivity,  $\bar{\sigma}$ , of an acoustic metal cannot be arbitrarily large. As proven in Appendix B, it is constrained by the given volume because of the principle of causality<sup>19</sup>. To be specific, for any structure targeting a constant  $\bar{\sigma}$  over a broadband frequency regime, causality dictates that its volume,  $V$ , must have a minimum volume requirement:

$$V \geq \bar{\sigma} Z_0 \frac{a}{\pi^2} \int_0^{\infty} \ln \left| \frac{1+\zeta}{1-\zeta} \right| d\lambda = V_{\min}, \quad (6)$$

where,  $\lambda = 2\pi c/\omega$  the wavelength and  $\zeta = 2i\omega\delta\omega/\pi \times \sum_n 1/(\omega_n^2 - \omega^2 - i\omega\beta_n)$  for the structures of our design. According to Equation (6),  $V_{\min}$  is proportional to  $\bar{\sigma} Z_0$  as shown

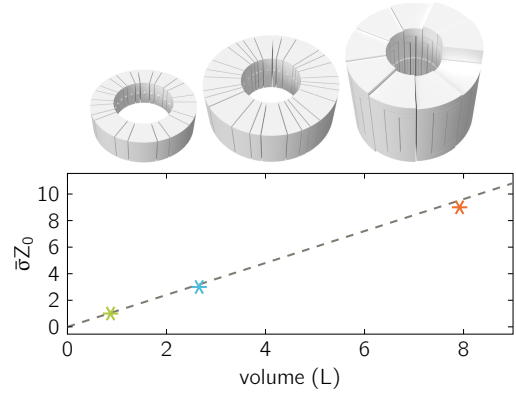


FIG. 4. Required volume for an acoustic metal. According to Equation (6), the principle of causality dictates a minimum volume for an acoustic metal that is proportional to its target  $\bar{\sigma} Z_0$  as shown by the dashed line. We have verified the relation by checking the volumes (stars) of three different experimental samples targeting  $\bar{\sigma} Z_0 = 1, 3, 9$  in the same frequency range of (290,625) Hz.

in Figure 4 by the dashed line. Therefore, a PAM of  $\bar{\sigma} \rightarrow \infty$  over a finite bandwidth will need an infinitely large volume, hence impossible in practice. It is worth to mention that the result of causality constraint in Ref. 19 is a specific case of Equation (6) with  $\bar{\sigma} Z_0 = 1$  and  $2a = \sum_n a_n$ .

We can experimentally verify Equation (6) by checking the volumes of different samples. To do so, we fabricated another two (the schematics in Figure 4) with smaller conductivities:  $\bar{\sigma} = 3/Z_0$  and  $\bar{\sigma} = 1/Z_0$  (impedance-matching). If we compare the real volumes,  $V$ , of all the three samples (stars) with  $V_{\min}$ , it is clear that they are very close to this causally optimal limit. Hence, they exhibit the linear relationship seen in Figure 4.

A useful approximation of Equation (6) (detailed in Appendix B) is given by

$$V \simeq V_{\min} \simeq \bar{\sigma} Z_0 \frac{2a}{\pi^2} (\lambda_1 - \lambda_N), \quad (7)$$

in which,  $\lambda_{1(N)} = 2\pi c/\omega_{1(N)}$  are the wavelengths at the lower and upper bounds of the designed frequency band. Take our first sample as an example,  $\bar{\sigma} Z_0 = 9$  within the band (290,625) Hz, so that  $2\bar{\sigma} Z_0 (\lambda_1 - \lambda_N)/\pi^2$  gives an effective length about 1.1 m and, for the duct of cross-sectional area  $a = 7.85 \times 10^{-3} \text{ m}^2$ ,  $V \simeq 8.64 \text{ L}$  that is quite close to the sample's real volume of 7.92 L.

## VI. CONCLUSION

We have realised the acoustic counterpart of EM wave's metallic behaviour by integrating an array of HR resonators each with a large dissipative coefficient. Instead of absorbing the acoustic energy, the composite array strongly reflects sounds within an octave (from 290 to 625 Hz). A circular ring of acoustic metal lining the inner wall of an air duct blocks 99% of the noise energy within a distance 1/30 of the longest wavelength, without impeding the airflow. One can therefore



$n$	1	2	3	4	5	6	7	8	9
$\omega_n/\omega_1$	1	1.03	1.09	1.12	1.17	1.22	1.28	1.32	1.36
$a_n(\text{cm}^2)$	4.27	4.48	4.45	4.27	4.13	4.13	3.79	3.79	3.68
$A_n/a_n$	18	16	16	15	14	14	13	13	12
$n$	10	11	12	13	14	15	16	17	18
$\omega_n/\omega_1$	1.41	1.46	1.50	1.53	1.57	1.61	1.66	1.70	1.75
$a_n(\text{cm}^2)$	3.50	3.50	3.44	3.44	3.44	3.38	3.41	3.41	3.26
$A_n/a_n$	12	11	10	10	10	9.5	9.2	8.6	8.7
$n$	19	20	21	22	23	24	25	26	27
$\omega_n/\omega_1$	1.80	1.84	1.88	1.93	1.97	2.02	2.05	2.10	2.16
$a_n(\text{cm}^2)$	3.33	3.30	3.28	3.26	3.52	3.54	4.69	4.66	4.62
$A_n/a_n$	8.2	7.9	7.5	7.3	6.9	6.6	4.5	4.3	4.1

TABLE I. The resonance frequencies and geometric parameters of the 27 HRs. The frequencies are normalised to the resonance of the first HR,  $\omega_1 = 290 \times 2\pi$  Hz and fairly evenly distributed.  $a_n$  and  $A_n$  are the areas of neck and cavity of the  $n$ th HR respectively.

expect its application to effectively reduce noise generated by fans and heavy machinery (as shown in Appendix C and the Supplementary demo video). We further delineate the causality constraint on absorption<sup>19,20</sup> to acoustic metals. The proposed novel acoustic material properties enrich the possibilities for new types of insertion loss panels<sup>32-39</sup>. In particular, features such as large bandwidth, low spectral dispersion, and high susceptibility are critical for many acoustic elements such as absorbers, lenses, and audio devices<sup>40</sup>.

### ACKNOWLEDGMENTS

M.Y. wishes to acknowledge the help by Ping Sheng for the inspiring discussions and numerous suggestions during the preparation and revision of the manuscript. M.Y. and M.X. wish to thank Bin Liang, Jing Yang, and Caixing Fu for helpful discussions. M.X. and Y.X. wish to thank Chui Yan Chan, Hin Chi Wong, Ming To Wong, and Man Ying Liew for their assistance in sample preparations and testing, and Shenzhen WeNext Technology for their 3D-printing support.

### Appendix A: Supplementary Note for the Design Methodology

Figure 5a is a schematic drawing for a single HR used in our design. For the  $n$ th one, we denote the area of its opening (red) as  $a_n$ . If the volume of the sector-cylindrical cavity is  $V_n$  and the depth along the radius is  $L$ , we can define its effective area  $A_n = V_n/L$  (green). In our case, the length of neck is  $l = 2$  mm and  $L = 74$  mm, the resonance frequencies,  $\omega_n$ , of the 27 HRs together with the associated  $a_n$  and  $A_n$  are listed in Table I. Here, the values of  $\omega_n$  were from the FEM simulation by COMSOL Multiphysics, in which the evanescent waves at the openings and the weak couplings between neighbouring HRs have all been included.

Unlike the Lorentz resonator whose response was always suppressed by the damping mechanism, our proposed acoustic

metal can have large damping while simultaneously display large displacement velocity. Here, we will try to visualise this fact by drawing the  $\tilde{v}$  of our sample in the phase-diagram, as shown by the top row in Figure 5b, when the damping coefficient  $\beta$  takes values from  $0.02\delta\omega$  to  $20\delta\omega$ . It is clear that the overall motion intensities of  $\tilde{v}$  increase if  $\beta < 2\delta\omega$  and only start to drop when  $\beta > 2\delta\omega$ . Therefore, we have chosen the value of  $2\delta\omega$  for  $\beta$  in the design.

On the contrary, if we block all the other 26 resonators and leave only one open (e.g., the 14th one), there is only one term left in the summation in Equation (5a) and the relevant responded velocity has a simple Lorentz-form (as shown in Figure 3f),

$$\tilde{v}_{14} = \frac{-72i\omega\delta\omega a/(\pi\rho c a_{14})}{\omega_{14}^2 - \omega^2 - i\omega(\beta + 18\delta\omega/\pi)} p_i. \quad (\text{A1})$$

The bottom row of Figure 5b shows that, in contrast to what happened in our acoustic metal, its magnitude continuously shrinks as the growth of  $\beta$ .

We also wish to show the role of the mode-density in the acoustic metal by a series of numerical examples. Let's start from 20 resonators uniformly distributed in an octave,  $(\omega_1, 2\omega_1)$ . Their  $f_n = 2\omega_1 a/(19\pi\rho c a_n)$  and  $\beta = 2/19 \times \omega_1$  so that meet the requirement of a good broadband absorber. Figure 5c shows its complex  $\tilde{v}$  in the phase-diagram together with the reflected energy ratio  $|r|^2$  and phase  $\angle r$  under normal incident sounds. Nearly perfect absorption,  $|r|^2 \sim 0$ , is seen in the design band but  $\angle r$  is away from  $\pi$ . Now, if we keep increasing the number of resonators,  $N$ , within the same frequency range,  $\tilde{v}$  starts to move along the small red arrows in the phase-diagram and continue to converge towards the PAM limit, as illustrated in Figures 5d and e. Eventually,  $|r|^2 \rightarrow 1$  and  $\angle r \rightarrow \pi$ .

The above phenomenon recalls for us an optical analogy in the drying of a drop of ink. As shown in Figure 5f, during the process of its drying, a drop of red ink on glass starts to acquire a metallic greenish reflection, sometimes called “sheen”. The reason is that the red ink absorbs out the greens of transmitted light. So if the ink is very concentrated, the number of dye particles per unit volume will be large and can therefore exhibit a strong surface reflection for the frequencies of green light—similar as what we have seen in the above simulations for sounds. That means, the mechanism in this paper is not limited to acoustics as concluded by Richard Feynman as “if any material gets to be a very good absorber at any frequency, the waves are strongly reflected at the surface and very little gets inside to be absorbed.”<sup>41</sup>

Finally, let's evaluate  $Z_0$  of a narrow duct for the array of objects on the sidewalls. By a “narrow” duct, we mean one whose width is small comparing to the wavelengths. So that only the waves with uniform front can travel inside. For the array also small along the wave direction, the air region in front of it is in sub-wavelength hence relatively incompressible. That means the net volume of air in and out of it is zero. Mathematically,  $\sum_n a_n v_n + 2av_{\text{rad}} = 0$  with  $v_{\text{rad}}$  being the particle displacement velocity of the pair of symmetric radiative sound waves pointing outward. For a given objects' motions of  $v_n$  that cause a sound pressure in the front air by  $p_{\text{rad}}$ ,

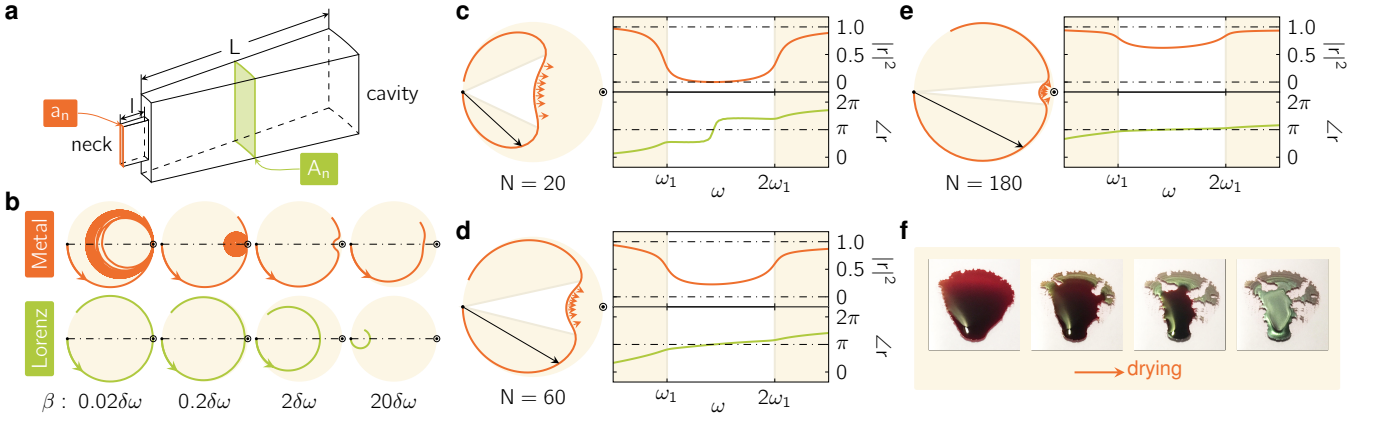


FIG. 5. Supplementary to the design methodology. **a**, The schematic drawing of a single HR in our acoustic metal. **b**, Comparison between the acoustic metal and a Lorentzian resonator under varying system damping coefficients  $\beta$ . The curves are the trace of their  $\tilde{v}$  in the phase-diagram as the frequency increases (along the direction denoted by the arrow). **c-e**, Different absorbers comprise the different number of resonators,  $N$ , distributed in the same frequency range ( $\omega_1, 2\omega_1$ ). On the left columns are their complex  $\tilde{v}$  on the phase-diagram. On the right are the relevant reflection intensity  $|r|^2$  and phase  $\angle r$  under normal incidents. The sectors and bands without any shading represent the designed frequency band. **f**, The photo of a drop of red ink on glass at different times during its drying.

$v_{\text{rad}} = p_{\text{rad}}/(\rho c)$  so that  $\sum_n a_n v_n = -2ap_{\text{rad}}/(\rho c)$ . Therefore, according to the definition,

$$Z_0 \equiv -\frac{p_{\text{rad}}}{\tilde{v}} = \frac{\sum_n a_n}{2a} \rho c. \quad (\text{A2})$$

For a pair of symmetrically incident sound waves in the same amplitude and phase, the relevant symmetric reflections from the array are given by

$$p_r^+ = \frac{1/(\bar{\sigma} - i\omega\bar{\epsilon}) - Z_0}{1/(\bar{\sigma} - i\omega\bar{\epsilon}) + Z_0} p_i^+. \quad (\text{A3})$$

Here, we use the superscript + to denote the symmetric feature. Meanwhile, anti-symmetric incidents will not excite the motions of the array, hence the anti-symmetric  $p_r^- = -p_i^-$ .

The scenario of sound coming from one side is the superposition of the symmetric and anti-symmetric scattering processes equally weighted:<sup>19</sup>  $p_i = p_i^+ + p_i^-$  and  $p_i^+ = p_i^-$ . Therefore, the transmitted and reflected sounds are given by

$$p_t = p_r^+ - p_r^- = \frac{1/(\bar{\sigma} - i\omega\bar{\epsilon})}{1/(\bar{\sigma} - i\omega\bar{\epsilon}) + Z_0} p_i, \quad (\text{A4a})$$

$$p_r = p_r^+ + p_r^- = \frac{-Z_0}{1/(\bar{\sigma} - i\omega\bar{\epsilon}) + Z_0} p_i, \quad (\text{A4b})$$

or, in terms of  $\tilde{v}$ ,

$$p_t = \left(1 - \frac{\tilde{v}}{2}\right) p_i, \text{ and } p_r = -\frac{\tilde{v}}{2} p_i. \quad (\text{A5})$$

Because there is always half of the energy in the incoming sound cannot be coupled to the objects, the maximum of their absorption coefficient can only be  $A_{\text{max}} = 0.5$ .

## Appendix B: Volume Requirement from Causality Principle

To explore the role of causality in acoustic metals, we consider a thought experiment of embedding the sample in an

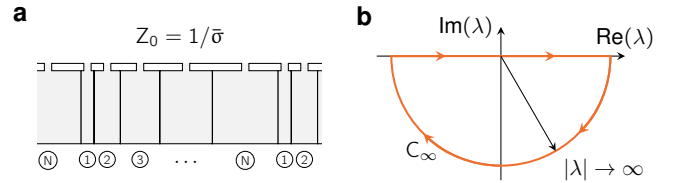


FIG. 6. **a**, Schematics for the thought experiment to explore the causality constraint. The composite was placed in an imaginary medium having the specific impedance  $Z_0 = 1/\bar{\sigma}$  with  $\bar{\sigma}$  being its target conductivity (inside of the cavities are still air shown in grey). **b**, The contour for the integral in Equation (B4).

imaginary medium having the specific impedance  $Z_0 = 1/\bar{\sigma}$ , the reciprocal of the target acoustic conductivity  $\bar{\sigma}$  (as shown in Figure 6a). The reflection process in this thought experiment should also follow the principle of causality hence constrained in a similar way as shown in Ref. 20. That means,

$$p_r(t) = \int_{-\infty}^{\infty} r(\delta t) p_i(t - \delta t) d\delta t. \quad (\text{B1})$$

with  $r(\delta t) = 0$  when  $\delta t < 0$ . Therefore, the reflection coefficient as a function of frequency,

$$r(\omega) = \int_{-\infty}^{\infty} r(\delta t) e^{i\omega\delta t} d\delta t, \quad (\text{B2})$$

can be analytically continued into the complex frequency and still be analytic in the upper half-plane. In terms of the wavelength  $\lambda = 2\pi c/\omega$ , that means  $r(\lambda)$  has no poles in the lower half-plane of complex  $\lambda$  but may have zeros. Similar as in Ref. 20, we consider the logarithmic function  $\ln r$  which is analytic except in the positions,  $\lambda_n$ , where  $r = 0$ . Such logarithmic singularities can be removed by multiplying the factor  $(\lambda - \lambda_n^*)/(\lambda - \lambda_n)$  with unity amplitude, where, \* denotes the

complex conjugation. Then for

$$\tilde{r}(\lambda) = r(\lambda) \prod_n \frac{\lambda - \lambda_n^*}{\lambda - \lambda_n}, \quad (\text{B3})$$

$\ln \tilde{r}(\lambda)$  is analytic with no singularities in the lower half-plane.

Therefore, according to the Cauchy's theorem, the integral along the contour in Figure 6b is zero,

$$\int_C \ln \tilde{r} d\lambda = 0. \quad (\text{B4})$$

Because  $|\tilde{r}| = |r|$  and  $|r(\lambda)| = |r(-\lambda)|$ , the real part of Equation (B4) gives

$$\begin{aligned} & -2 \int_0^\infty \ln |r| d\lambda \\ & = \text{Re} \left[ \int_{C_\infty} \left( \ln r + \sum_n \ln \frac{\lambda - \lambda_n^*}{\lambda - \lambda_n} \right) d\lambda \right], \end{aligned} \quad (\text{B5})$$

here  $C_\infty$  is a lower half-circle with radius tends to infinity.

In the long wavelength limit of  $|\lambda| \rightarrow \infty$ ,

$$\lim_{|\lambda| \rightarrow \infty} \ln \frac{\lambda - \lambda_n^*}{\lambda - \lambda_n} = 2i \frac{\text{Im}(\lambda_n)}{\lambda} \quad (\text{B6})$$

so that

$$\int_{C_\infty} \ln \frac{\lambda - \lambda_n^*}{\lambda - \lambda_n} d\lambda = 2\pi \text{Im}(\lambda_n). \quad (\text{B7})$$

Where,  $\int_{C_\infty} d\lambda = \int_0^{-\pi} i\lambda d\gamma$  with  $\lambda = |\lambda|e^{i\gamma}$ . Meanwhile, when  $\lambda \rightarrow \infty$ , the composite was uniformly compressed and expanded under the external pressure  $p_i + p_r$ . According to Hooke's law,  $p_i + p_r = \kappa_0 \Delta V/V = i\kappa_0 \bar{v} \sum_n a_n / (\omega V)$  with  $\kappa_0$  the static bulk modulus of the composite and  $V$  their total volume. On the other hand, since  $\bar{v} = (p_i - p_r)/Z_0 = \bar{\sigma}(p_i - p_r)$ , the reflection coefficient can be solved as

$$\begin{aligned} r &= \frac{p_r}{p_i} = \frac{\kappa_0 \bar{\sigma} \sum_n a_n + i\omega V}{\kappa_0 \bar{\sigma} \sum_n a_n - i\omega V} = 1 + i \frac{1}{\kappa_0 \bar{\sigma}} \frac{2V}{\sum_n a_n} \omega + \dots \\ &= 1 + i \frac{\kappa}{\kappa_0 \bar{\sigma} \rho c} \frac{4\pi V}{\sum_n a_n \lambda} + \dots, \end{aligned} \quad (\text{B8})$$

here  $\kappa = \rho c^2$  denotes the air bulk modulus. Hence,  $\ln r \simeq i\kappa/\kappa_0 \times 4\pi V / (\bar{\sigma} \rho c \sum_n a_n \lambda)$  at the long wavelength limit and  $\int_{C_\infty} \ln r d\lambda = \kappa/\kappa_0 \times 4\pi^2 V / (\bar{\sigma} \rho c \sum_n a_n)$ . Therefore,

$$\begin{aligned} - \int_0^\infty \ln |r| d\lambda &= \frac{\kappa}{\kappa_0 \bar{\sigma} \rho c} \frac{2\pi^2 V}{\sum_n a_n} + \pi \sum_n \text{Im}(\lambda_n) \\ &\leq \frac{\kappa}{\kappa_0 \bar{\sigma} \rho c} \frac{2\pi^2 V}{\sum_n a_n} \end{aligned} \quad (\text{B9})$$

since  $\text{Im}(\lambda_n) \leq 0$ .

For our acoustic metal, according to Equation (4),

$$\tilde{v} = 2 \left[ 1 + \frac{\sum_n a_n}{i\omega Z_0} \left( \sum_n \frac{a_n f_n}{\omega_n^2 - \omega^2 - i\omega \beta_n} \right)^{-1} \right]^{-1} \quad (\text{B10})$$

in the current case,  $Z_0 = 1/\bar{\sigma}$ , and

$$r = 1 - \tilde{v} = \frac{1 + \zeta}{1 - \zeta} \quad (\text{B11})$$

with

$$\zeta = \frac{i\omega}{\bar{\sigma} \sum_n a_n} \sum_n \frac{a_n f_n}{\omega_n^2 - \omega^2 - i\omega \beta_n}. \quad (\text{B12})$$

Because  $f_n = 2\bar{\sigma} \delta\omega \sum_n a_n / (\pi a_n)$ ,

$$\zeta = i \frac{2\omega \delta\omega}{\pi} \sum_n \frac{1}{\omega_n^2 - \omega^2 - i\omega \beta_n} \quad (\text{B13})$$

irrelevant to the target  $\bar{\sigma}$ . Also, if the composite was rigid cavities filled with air as what in the main text,  $\kappa_0 = \kappa$ , Equation (B9) becomes

$$V \geq \bar{\sigma} \rho c \frac{\sum_n a_n}{2\pi^2} \int_0^\infty \ln \left| \frac{1 + \zeta}{1 - \zeta} \right| d\lambda. \quad (\text{B14})$$

That gives a lower limit for the volume proportional to  $\bar{\sigma}$ .

To further evaluate the integral in Equation (B14), we assume that the system's averaged acoustic conductivity ideally takes the value of  $\bar{\sigma}$  within the frequency range  $(\omega_1, \omega_N)$  and being zero elsewhere. According to the Kramers-Kronig relationship,

$$\bar{\sigma} - i\omega \bar{\epsilon} = -i \frac{2\bar{\sigma}}{\pi} \left[ \tanh^{-1} \frac{\omega_1}{\omega} - \tanh^{-1} \frac{\omega_N}{\omega} \right]. \quad (\text{B15})$$

The substitution of Equation (B15) into Equation (B11) gives

$$r = \frac{i\pi/2 - \tanh^{-1}(\lambda/\lambda_1) + \tanh^{-1}(\lambda/\lambda_N)}{i\pi/2 + \tanh^{-1}(\lambda/\lambda_1) - \tanh^{-1}(\lambda/\lambda_N)} \quad (\text{B16})$$

with  $\lambda_{1(N)} = 2\pi c/\omega_{1(N)}$ . Its substitution into Equation (B14) gives

$$V \geq \bar{\sigma} \rho c \frac{\sum_n a_n}{\pi^2} (\lambda_1 - \lambda_N). \quad (\text{B17})$$

The above equation can provide an estimate for the volume of an acoustic metal based only on the knowledge of the target conductivity and bandwidth. Usually, this estimate will be a little bit higher than the volume's actual lower limit, since Equation (5a) cannot so perfectly match the target in practice.

### Appendix C: Applications in Ventilation Noise Reduction

The understanding about the causality constraint provides us with a new perspective for the application of noise control. According to Equation (B17), the better blocking efficiency in an air duct, that corresponds to larger values of  $\bar{\sigma}$ , requires larger volume of  $V$ . However, in practice, there is usually limited volume available for the noise treatments. In this case, the spectrum design becomes crucial, with which one can design the reflection ability given by a volume to concentrate in the frequencies where the noise energy is most intensive, so as to

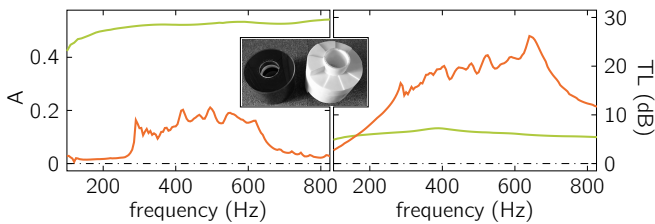


FIG. 7. The comparison of absorption coefficient ( $A$ ) and the transmission loss (TL) between our composite liner (red) and the traditional one of acoustic foam (green). All the data are from the experiments. The inset is the photo of the two samples. From the two plots it is clear that whereas acoustic foam is mostly an absorptive material, our acoustic metal displays superior transmission loss with low dissipation.

narrow the bandwidth in Equation (B17) for a larger  $\bar{\sigma}$  of better noise reduction effect. This strategy is particularly useful for the noise having a characteristic spectrum, such as from the fan and machine.

To demonstrate the advantage of our spectrum design, we have compared our composite liner with a traditional one which comprises an acrylic cavity filled by acoustic foam, as shown by the inset photo in Figure 7. The volume of the cavity

is the same as our sample and connected to the air duct by the same necks. As shown in the right column of Figure 7, such a liner exhibited even transmission loss (TL) about 5 (dB) for all the measuring frequencies. In contrary, the TL of our liner was maximised within the design band of (290, 625) Hz and presented the advantages of 10 ~ 20 dB.

In acoustics, acoustic foam has been generally considered as a high dissipative material. However, as mentioned at the beginning of this paper, the associated damping is not large enough for being an acoustic metal. That is evidenced by the absorption data as shown in Figure 7. The absorption coefficient  $A = 1 - |t|^2 - |r|^2 \sim 0.5$  indicated that the relevant effective acoustic conductance was only  $\bar{\sigma}Z_0 \simeq 1$ . Which is far below the  $\bar{\sigma}Z_0 = 9$  of our sample.

To show the sound blocking effect of acoustic metal, we have made a demo video in the Supplementary Material in which, a Bluetooth speaker, playing an audio recording of broadband wind noise, was placed at the bottom of the air duct with the HRs' openings closed by a metallic ring. The loud noise can be heard at the top port. A Decibel meter near the top port recorded a sound pressure level (SPL) at 95 dB. After removing the metallic ring to expose the HRs to the noises, the emitted SPL suddenly drops to 70 dB. This contrast evidenced a very significant 25 dB of the TL for the specific wind noise.

\* Correspondence email: min@metacoust.com

† Correspondence email: chen@metacoust.com

<sup>1</sup> E. Hagen and H. Rubens, *Annalen der Physik* **316**, 873 (1903).

<sup>2</sup> S. A. Cummer, J. Christensen, and A. Alù, *Nature Reviews Materials* **1**, 1 (2016).

<sup>3</sup> G. Ma and P. Sheng, *Science advances* **2**, e1501595 (2016).

<sup>4</sup> M. Kadic, G. W. Milton, M. van Hecke, and M. Wegener, *Nature Reviews Physics* **1**, 198 (2019).

<sup>5</sup> B. Assouar, B. Liang, Y. Wu, Y. Li, J.-C. Cheng, and Y. Jing, *Nature Reviews Materials* **3**, 460 (2018).

<sup>6</sup> Z. Liu, X. Zhang, Y. Mao, Y. Zhu, Z. Yang, C. T. Chan, and P. Sheng, *science* **289**, 1734 (2000).

<sup>7</sup> N. Fang, D. Xi, J. Xu, M. Ambati, W. Srituravanich, C. Sun, and X. Zhang, *Nature materials* **5**, 452 (2006).

<sup>8</sup> S. H. Lee, C. M. Park, Y. M. Seo, Z. G. Wang, and C. K. Kim, *Physical review letters* **104**, 054301 (2010).

<sup>9</sup> V. C. Nguyen, L. Chen, and K. Halterman, *Physical review letters* **105**, 233908 (2010).

<sup>10</sup> M. Yang, G. Ma, Z. Yang, and P. Sheng, *Physical review letters* **110**, 134301 (2013).

<sup>11</sup> Y. Xie, B.-I. Popa, L. Zigoneanu, and S. A. Cummer, *Physical review letters* **110**, 175501 (2013).

<sup>12</sup> N. Kaina, F. Lemoult, M. Fink, and G. Lerosey, *Nature* **525**, 77 (2015).

<sup>13</sup> T. Frenzel, M. Kadic, and M. Wegener, *Science* **358**, 1072 (2017).

<sup>14</sup> Z. Rueger and R. Lakes, *Physical review letters* **120**, 065501 (2018).

<sup>15</sup> H. Zhu, J. Yi, M.-Y. Li, J. Xiao, L. Zhang, C.-W. Yang, R. A. Kaindl, L.-J. Li, Y. Wang, and X. Zhang, *Science* **359**, 579 (2018).

<sup>16</sup> R. Fleury, D. L. Sounas, C. F. Sieck, M. R. Haberman, and A. Alù, *Science* **343**, 516 (2014).

<sup>17</sup> Y. Aurégan and V. Pagneux, *Physical review letters* **118**, 174301

(2017).

<sup>18</sup> R. Fleury, D. L. Sounas, and A. Alù, *Physical Review B* **91**, 174306 (2015).

<sup>19</sup> M. Yang and P. Sheng, *Annual Review of Materials Research* **47**, 83 (2017).

<sup>20</sup> M. Yang, S. Chen, C. Fu, and P. Sheng, *Materials Horizons* **4**, 673 (2017).

<sup>21</sup> C. Zhang and X. Hu, *Physical Review Applied* **6**, 064025 (2016).

<sup>22</sup> L.-j. Li, B. Zheng, L.-m. Zhong, J. Yang, B. Liang, and J.-c. Cheng, *Applied Physics Letters* **113**, 103501 (2018).

<sup>23</sup> X. Peng, J. Ji, and Y. Jing, *The Journal of the Acoustical Society of America* **144**, EL255 (2018).

<sup>24</sup> H. Chang, L. Liu, C. Zhang, and X. Hu, *AIP Advances* **8**, 045115 (2018).

<sup>25</sup> Y. Zhu, K. Donda, S. Fan, L. Cao, and B. Assouar, *Applied Physics Express* **12**, 114002 (2019).

<sup>26</sup> C. R. Liu, J. H. Wu, F. Ma, X. Chen, and Z. Yang, *Applied Physics Express* **12**, 084002 (2019).

<sup>27</sup> H. Long, C. Shao, C. Liu, Y. Cheng, and X. Liu, *Applied Physics Letters* **115**, 103503 (2019).

<sup>28</sup> S. Huang, Z. Zhou, D. Li, T. Liu, X. Wang, J. Zhu, and Y. Li, *Science Bulletin* **65**, 373 (2020).

<sup>29</sup> J. D. Jackson, "Classical electrodynamics," (John Wiley&Sons, 1999) Chap. 7.5C, 3rd ed.

<sup>30</sup> M. Yang, G. Ma, Y. Wu, Z. Yang, and P. Sheng, *Physical Review B* **89**, 064309 (2014).

<sup>31</sup> For  $\delta\omega \rightarrow 0$ , the summation in Equation (5a) becomes an integral similar to that in Equation (3b) of Ref. 20 whose result, in which  $D(\omega) = 1/\delta\omega$  and  $Z_{\text{tar}} = 1/\bar{\sigma}$ , is the basis of our design.

<sup>32</sup> G. Ma, M. Yang, Z. Yang, and P. Sheng, *Applied Physics Letters* **103**, 011903 (2013).

<sup>33</sup> M. Yang, C. Meng, C. Fu, Y. Li, Z. Yang, and P. Sheng, *Applied*



- Physics Letters **107**, 104104 (2015).
- <sup>34</sup> Y. Cheng, C. Zhou, B. Yuan, D. Wu, Q. Wei, and X. Liu, *Nature materials* **14**, 1013 (2015).
- <sup>35</sup> H.-l. Zhang, Y.-f. Zhu, B. Liang, J. Yang, J. Yang, and J.-c. Cheng, *Applied Physics Letters* **111**, 203502 (2017).
- <sup>36</sup> X. Wu, K. Y. Au-Yeung, X. Li, R. C. Roberts, J. Tian, C. Hu, Y. Huang, S. Wang, Z. Yang, and W. Wen, *Applied Physics Letters* **112**, 103505 (2018).
- <sup>37</sup> R. Ghaffarivardavagh, J. Nikolajczyk, S. Anderson, and X. Zhang, *Physical Review B* **99**, 024302 (2019).
- <sup>38</sup> G.-S. Liu, Y. Zhou, M.-H. Liu, Y. Yuan, X.-Y. Zou, and J.-C. Cheng, *Scientific Reports (Nature Publisher Group)* **10** (2020).
- <sup>39</sup> H. Nguyen, Q. Wu, X. Xu, H. Chen, S. Tracy, and G. Huang, *Applied Physics Letters* **117**, 134103 (2020).
- <sup>40</sup> S. Degraeve and J. Oclec-Brown, in *Audio Engineering Society Convention 148* (Audio Engineering Society, 2020).
- <sup>41</sup> R. P. Feynman, R. B. Leighton, and M. Sands, "The feynman lectures on physics, volume 2," (Pearson Addison Wesley, 2006) Chap. 33-5, definitive edition ed.